This article has been accepted for publication in a future issue of this journal, but has not been fully edited. Content may change prior to final publication. Citation information: DOI 10.1109/TUFFC.2021.3086597, IEEE Transactions on Ultrasonics, Ferroelectrics, and Frequency Control

High Frame Rate Volumetric Imaging of Microbubbles Using a Sparse Array and Spatial Coherence Beamforming

Luxi Wei[1], Geraldi Wahyulaksana[1], Bram Meijlink[1], Alessandro Ramalli[2], Emile Noothout[3], Martin Verweij[3], Enrico Boni[2], Klazina Kooiman[1], Antonius F.W. van der Steen[1], Piero Tortoli[2], Nico de Jong[1,3], Hendrik J. Vos[1,3]

[1]Biomedical Engineering, Erasmus MC, University Medical Center Rotterdam, Department of Cardiology, Rotterdam, the Netherlands. [2]Department of Information Engineering, University of Florence, Florence, Italy. [3]ImPhys, Delft University of Technology, Delft, the Netherlands

***Abstract*— Volumetric ultrasound imaging of blood flow with microbubbles enables more complete visualization of the microvasculature. Sparse arrays are ideal candidates to perform volumetric imaging at reduced manufacturing complexity and cable count. However, due to the small number of transducer elements, sparse arrays often come with high clutter levels, especially when wide beams are transmitted to increase the frame rate. In this study, we demonstrate with a prototype sparse array probe and a diverging wave transmission strategy, that a uniform transmission field can be achieved. With the implementation of a spatial coherence beamformer, background clutter signal can be effectively suppressed, leading to a signal to background ratio improvement of 25 dB. With this approach, we demonstrate the volumetric visualization of single microbubbles in a tissue-mimicking phantom as well as vasculature mapping in a live chicken embryo chorioallantoic membrane.**

***Index Terms*—Coherence beamforming, volumetric imaging, high frame rate, microbubbles, sparse array.**

I. INTRODUCTION

Microbubbles have been widely used as an ultrasound contrast agent in the clinic, and have been shown as an excellent diagnostic tool [1]–[4]. When imaged at high frame rates, advanced post-processing filters and microbubble-specific pulsing sequences allow differentiation of contrast and tissue signal, enabling 2-dimensional (2-D) microvasculature mapping and blood flow measurements *in vivo* [5], [6].

Recent developments in matrix arrays have led to high volume rate 3-dimensional (3-D) imaging for a more complete picture of the microvasculature [7], [8]. Fully populated matrix arrays can reach relatively high contrast and high frame rates, but current solutions are impractical for clinical use because of the amount of probe connection cables, the requirement of multiple systems and their mutual data synchronization [9], [10]. To circumvent these issues while still retaining the high element count, more complex read-out sequences have been proposed, such as application specific integrated circuits (ASICs) for in-probe sub-aperture beamforming and switching [11]–[13], a row-column addressing scheme [14], [15] or multiplexed array sequences [16], [17]. However, all of these methods have inherent drawbacks in terms of costs, stitching, or limited frame rate due to switching or volumetric beam scanning.

As an alternative, channel count and electronic complexity can be reduced by sparsely distributing the elements in a 2D array. Ramalli *et al.* have proposed a tapered spiral pattern of 256 elements, which can have one-to-one connections to an ultrasound system, allowing full control of the transmitted beams and received signals [18], albeit potentially at the cost of lower signal-to-noise ratio (SNR). This array configuration has been used in combination with multi-line and multi-plane transmits [19] to evaluate the effects of each modality on image quality and signal-to-noise ratio. Harput *et al.* have also shown the effectiveness of a 2-D density tapered array for 3-D, high frame rate, super-resolution imaging [20] and its suitability for quantitative micro-vessel analysis *in vitro* [21]. The sparse spiral array offers flexibility in transmission sequences, can perform high frame rate imaging, and has low electronics complexity and hardware requirements. These advantages make it a promising tool for high frame rate 3-D vasculature imaging.

For application in research and pre-clinical imaging, the use of sparse arrays with microbubble volumetric imaging is here investigated. This approach involves three main challenges to be faced: the low SNR, the non-uniformity of the transmitted field, and the high

This article has been accepted for publication in a future issue of this journal, but has not been fully edited. Content may change prior to final publication. Citation information: DOI 10.1109/TUFFC.2021.3086597, IEEE Transactions on Ultrasonics, Ferroelectrics, and Frequency Control

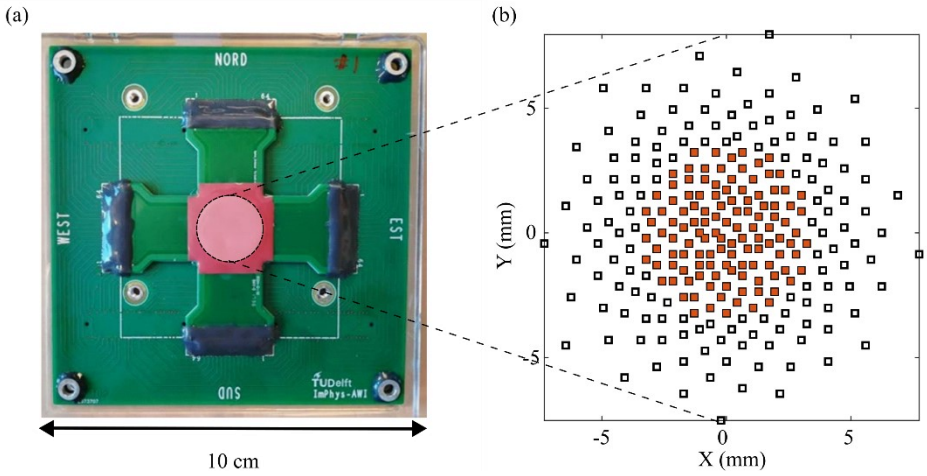

Fig. 1. (a) The front face of the prototype spiral array. The circled area in the center is populated with elements distributed as shown in (b). Only the center 120 (red) elements were used to transmit in the experiments, while all 256 elements were used in receive. Element size is not drawn to scale.

level of artefacts due to the spatial under-sampling of the received echoes, as discussed in the next paragraphs.

Low SNR levels is a fundamental limitation of sparse arrays [22]. Because of the few number of elements, the transmitted field pressure from the sparse array cannot reach the same levels as in its fully-populated counter-part. Yet, in case of *high frame rate* microbubble imaging, acoustic pressures need to remain low anyhow since microbubbles are insonified much more often than in a line-based imaging approach [6], [23], and therefore the lower transmitted fields pressure are still acceptable for contrast-enhanced imaging. The lower number of elements also leads to lower receive sensitivity. The obvious way of increasing the SNR is to do averaging or low-pass filtering over the subsequently acquired data. Yet, such filtering is limited to stationary or slowly moving targets and is not suitable for vascular imaging and therefore, alternatives need to be sought.

The sparsity in the transmission aperture, in combination with the collimated or diverging beams needed to maintain a high volumetric frame rate, lead to both a high variation of magnitude and pulse shape within the field (examples will be provided below) [22]. The uniformity of the transmit field can be synthetically improved with angular compounding, but at a cost of lower frame rates.

Lastly, strong clutter in receive is generated by high-level grating lobes from contrast agents and tissue when using conventional delay-and-sum (DAS) beamforming. While quasi-stationary tissue signal and clutter can be removed by slow time filtering of the radiofrequency (RF) data or by contrast specific detection schemes [24], *microbubble clutter* has similar temporal characteristics as the microbubble signal of interest, and therefore cannot be removed with these methods. High levels of microbubble clutter can severely degrade image contrast and create artefacts. Alternatively, microbubble clutter can also be reduced by coherent angular compounding. On the other hand, coherent compounding reduces the frame rate, which may lead to decorrelation in high flow rate scenarios. Although motion compensation techniques may help to partially solve this issue [25], they might suffer from the low-quality volumes produced by the sparse array and might not be fully effective. Moreover, artefacts may arise in complex and non-uniform propagation media, which might impact on the registration of images obtained at different steering angles and, thus, degrade the final compounded image [25], [26]. Coherence-based beamforming methods have been proposed to decrease side/grating lobes and noise levels in images. Stanziola *et al*. have proposed to use the cross-correlation of two separately DAS-beamformed images obtained with the same transmit pulse for flow detection [27]. Harput *et al*. have further implemented this method to volumetric super-resolution imaging of microbubbles using an array of 512 elements and two ultrasound open scanners [20]. Lediju *et al*. have proposed to use the coherency of signals received by nearby transducer elements to perform short lag spatial coherence (SLSC) beamforming [28]. They have shown that by adjusting the 'lags' used for spatial coherence calculation, background noise can be suppressed. With this method, ultrasound molecular imaging of microbubbles in 2-D and volumetric imaging can be

This article has been accepted for publication in a future issue of this journal, but has not been fully edited. Content may change prior to final publication. Citation information: DOI 10.1109/TUFFC.2021.3086597, IEEE Transactions on Ultrasonics, Ferroelectrics, and Frequency Control

achieved [29]–[31]. These methods have been developed for linear and (fully-populated) matrix arrays, and have yet to be implemented on sparse arrays.

In this work, we present the imaging system and pipeline based on the spatial coherence (SC) beamformer to achieve high frame rate volumetric imaging of microbubbles in phantom experiments and *in vivo* in the chicken embryo.

II. Theory and Methods

A. Prototype sparse spiral array

Fig. 1 shows the prototype piezoelectric sparse array based on a tapered spiral design [18], [32]. This array has an aperture size of 1.6 cm diameter, consists of 256 elements, and each element has a dimension of 200 x 200 µm. The array was manufactured [32] by depositing layers of acoustic stack material (including PZT, conductive glue, and matching layer material) onto a PCB, and finally diced into a grid with 220 µm pitch. The PCB allows electrical connections to the 256 active element locations. The elements were wired directly to the 256 channels of a Vantage 256 (Verasonics, Kirkland, WA, USA) open scanner [33]. The density of the elements decreases towards the edge of the aperture, according to a Blackman window, designed to reduce side-lobe levels. The spiral array operates at a center frequency of 5 MHz with 40% bandwidth. More detailed manufacturing specifications can be found in Vos *et al*. [32].

B. Transmission and reception strategy

Single-pulse detection at the fundamental frequency (combined with the SVD filter for tissue suppression) was chosen for this study because this scheme has previously been used in perfusion imaging [8], [20], [27]. Diverging waves at different steering angles were transmitted and the radiofrequency echoes were filtered, beamformed, then compounded (coherently for DAS). Diverging waves were designed to provide a uniform pressure wavefront and to reduce pulse shape non-uniformities, while maintaining a large field of view. Field II [34], [35] simulations were conducted to investigate the effects of changing the number of active transmit elements (or the active transmit aperture diameter), the diverging wave opening angle (2α), and the maximum steering angle used for compounding. To investigate the effects of angular compounding on the uniformity of the transmit field, the measured transmit field at the same locations for all steering angles were lined up in time based on their time-of-arrival and then coherently compounded. This 'synthetic transmit field' shows the characteristics of the effective transmit field post angular compounding. For the simulations, all elements were assumed to be identical and with no ringing. When transmitting a 3-cycle sinusoidal burst at 5-MHz and tapered with a Gaussian window, a good tradeoff was found for $2\alpha = 30°$, using the center 120 elements, corresponding to a 7 mm aperture, (Fig 1. b) and steering at maximum 5°. All elements were used on receive to maximize the receive sensitivity and image resolution. The final imaging sequence consisted of five divergent waves, fired at 8 kHz PRF with steering angles of 0° and 5° in both azimuth and elevation directions. This sequence was repeated at a rate of 1 kHz. The echo signals, received by all $N = 256$ elements, were acquired for 3.9 seconds (corresponding to 3900 consecutive volumes), and then beamformed and processed off-line for an output frame rate of 1 kHz. Table I contains a summary of the transmission parameters.

TABLE I

List of Parameters

Transmission parameters (all experiments)	
Transmission element number (#)	120
Reception element number, N (#)	256
Center frequency (MHz)	5
Pulse cycles (#)	3
Angular PRF (kHz)	8
Post-compounding frame rate (kHz)	1
Steering angles (azimuth, elevation °)	(0,0); (5,0); (0,5); (-5,0); (0,-5)
Opening angle (°)	30
Acquisition duration (s)	3.9
SVD filter parameters	
Ranks removed for 1-mm vessel (ensemble length = 3900)	1
Ranks removed for 200-µm vessel (ensemble length = 100)	1
Ranks removed for chicken embryo (ensemble length = 3900)	20
Beamforming parameters	
Voxel size for 1-mm vessel (wavelength)	0.5
Voxel size for 200-µm vessel (wavelength)	0.5
Voxel size for chicken embryo (wavelength)	1

This article has been accepted for publication in a future issue of this journal, but has not been fully edited. Content may change prior to final publication. Citation information: DOI 10.1109/TUFFC.2021.3086597, IEEE Transactions on Ultrasonics, Ferroelectrics, and Frequency Control

C. *Spatial coherence beamforming*

While microbubbles in blood act like point sources producing highly spatially coherent echoes, the surrounding tissue scatters incoherently, and lowers the spatial coherence of microbubbles [28]. To maximize microbubble signal coherence, the background signal (originating from PVA or tissue) was first removed by applying an SVD filter on pre-beamforming RF data for each steering angle separately [36]. A manually selected number of lower ranks (large singular values) was removed to attenuate the quasi-stationary tissue signal (Table I). Since there was no clear separation of singular values between bubble signal and noise at low microbubble concentrations, the smallest singular values were not removed.

Similar to DAS beamforming, for each sub-volumetric acquisition, dynamic receive focusing was applied to the channels obtaining a 'delayed matrix'. Then, for each voxel, the 'delayed' signal received by all element pairs are used to calculate an average spatial signal coherence (sc_{voxel}) [37]:

$$sc_{voxel} = \frac{\sum_{i=1}^{N-1}\sum_{l=1}^{N-i} s(i)s^*(i+l)}{\sum_{i=1}^{N}|s(i)|^2}, \qquad (1)$$

where $s(i)$ is the signal received by element i, l is the lag of elements ranging from 1 to N-1, and * indicates the complex conjugate. Equation (1) also corresponds to the normalized autocorrelation function, and the spatial coherence calculation was thus performed in the frequency domain for higher computational efficiency. This was performed for all transmission angles independently. The resulting voxel values were complex, and with their real parts ranging between -1 and 1. The frames were then averaged to form an angular compounded. Further averaging in time can be performed at this point to show the accumulation of bubble signal during the acquisition duration. Finally, since we expect positive correlation values with zero phase, only the real part of the averaged coherence was taken to be the image amplitude at the voxel and all negative coherence was set to zero. The final volumetric image was then normalized and log compressed for display. As a comparison, DAS volumes were also calculated by summing across the channels for the same delayed matrixes, normalized, and log compressed for display. All beamforming and post-processing were implemented in MATLAB (The Mathworks Inc., Natick, MA, USA). Dynamic receive focusing calculations were based on the UltraSound ToolBox [38].

D. *Straight vessel phantom experiments*

A diluted Definity® microbubble solution (Lantheus Medical Imaging Inc., N. Billerica, MA, USA) was injected into a 1 mm inner-diameter silicone tube embedded in a tissue-mimicking PVA phantom [39]. The flow rate was 300 µL/min (peak velocity = 12.7 mm/s laminar equivalent). The vessel was located between 2 and 4 cm depth with an angle of 60° with respect to the axis of the probe (Fig. 2 a). Data acquisition and post-processing parameters can be found in Table I.

Quantitative signal to background evaluations were performed on a data volume obtained as the average of 50 frames for both DAS (incoherent average) and SC beamformed volumes. This averaging was performed to remove the speckle pattern inside the vessel. Since the frame rate was relatively high with respect to the flow velocity, the 50 frames were spaced 10 ms apart (100 Hz) such that the speckle pattern changed sufficiently between frames. Contrast calculations were performed on 7 distinct 50 frames averaged volumes from the same acquisition. A cylindrical mask with a diameter of 1 mm was used to select the

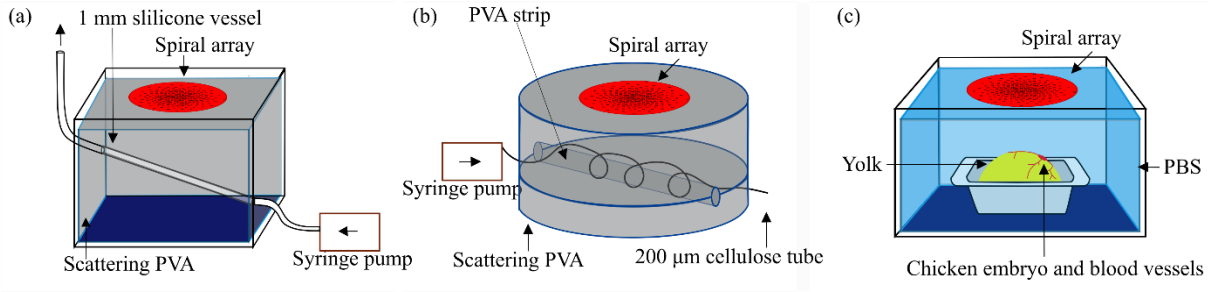

Fig. 2. Schematics of the (a) 1 mm straight vessel and (b) 200 µm helical vessel phantoms. The vessels were embedded in a tissue-mimicking PVA matrix. Experiments were performed with the spiral array placed on top of the phantoms. (c) Schematic of the chicken embryo setup. The chicken embryo and yolk are placed inside a 37° PBS bath after microbubble injection. The spiral array is placed on top of the bath, coupled to the chicken embryo through the PBS.

This article has been accepted for publication in a future issue of this journal, but has not been fully edited. Content may change prior to final publication. Citation information: DOI 10.1109/TUFFC.2021.3086597, IEEE Transactions on Ultrasonics, Ferroelectrics, and Frequency Control

microbubble signal within the vessel, and a cubic mask of the same volume was used to sample the background clutter signal (Fig. 4 a). The generalized contrast-to-background ratio (GCBR) was calculated as a quantitative metrics for the assessment of image quality. The GCBR is equivalent to the generalized contrast-to-noise ratio (GCNR) defined, in [40]. The new name is used here because in our case the background signal contains not only electronic noise but also clutter and grating lobes.

Once the probability distributions (i.e., the histograms) of both the vessel and the background signals were computed, the GCBR was defined as the non-overlapping (OVL: overlapping area) normalized area of the two distributions,

$$GCBR = 1 - OVL. \tag{3}$$

The signal to background ratio (SBR) was also computed in the angular compounding case using (4), where root mean square (RMS) values were calculated in the vessel and background regions of the linear envelope data.

$$SBR = 20\log_{10}\frac{RMS_{vessel}}{RMS_{background}}. \tag{4}$$

E. Helical micro-vessel phantom experiments

To create a micro-vessel phantom that includes flow in multiple directions, a helical shaped vessel phantom was designed using a 200 µm outer diameter cellulose tube embedded in a tissue-mimicking PVA matrix (Fig. 2 b). The inner diameter of the tube was optically measured to be between 150 µm and 180 µm. The micro-vessel was wrapped around a 5 mm diameter PVA cylinder, which was then placed in between two complimentary PVA slabs. A custom-made microbubble with a phospholipid coating and C_4F_{10} gas core (F type, mean diameter 1.1 µm, [41]) at low concentration was pumped into the cellulose tube at a constant flow rate of 25 µL/min (mean velocity = 16.5-23.6 mm/s laminar equivalent). Data acquisition and post-processing parameters can be found in Table I.

Single microbubbles were tracked to calculate their mean velocity. Microbubble identification and tracking in 3-D were performed using the algorithm presented in [42]. The localization steps include the segmentation of individual bubbles by masking based on voxel intensity, followed by the estimation of their center of mass. To further differentiate the bubble signal from noise, the Hungarian algorithm was used to track bubble motion through time, and the tracks were used to calculate bubble speed. For the visualization of the entire vessel, averaging was performed on the envelope-detected frames for the DAS volumes to avoid loss of coherence with the motion of the microbubbles. For the SC beamformed volumes, averaging was performed before removing negative coherence values. Averaged volumes from both beamforming methods were then normalized and log compressed.

F. Chicken embryo vascular imaging in vivo

A 5-day old chicken embryo was removed from its eggshell and placed in a plastic weighing boat (85 × 85 × 24 mm; VWR, the Netherlands) containing ~0.5 cm of ultrasound gel (Chemolan, Chemodis, Alkmaar, the Netherlands) on the bottom according to the protocol of Meijlink *et al.*[43]. Four µL of the custom-made bubble solution (F-type) was injected into the vascular

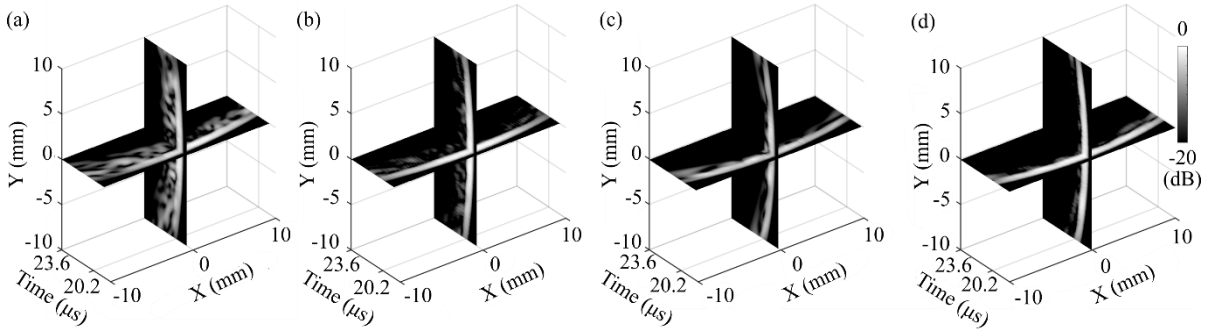

Fig. 3. Field II simulations of the one-way field obtained for 2*α = 30° divergent angle at 3 cm away from the transducer, displayed at a dynamic range of 20 dB normalized to their maximum amplitudes. (a) Transmitting with all elements. (b) Transmitting 5 partially overlapping beams with all elements. Four beams all with 5° steering angle were transmitted into different directions centered around a non-steered beam. The transmitted waves were simulated separately, corrected for time-of-flight differences and averaged, then mapped onto the wave-front locations of the non-steered transmit. (c) Transmitting one un-steered beam with the center 120 elements. (d) Transmitting with the center 120 elements and with the same steering configuration as in (b).

This article has been accepted for publication in a future issue of this journal, but has not been fully edited. Content may change prior to final publication. Citation information: DOI 10.1109/TUFFC.2021.3086597, IEEE Transactions on Ultrasonics, Ferroelectrics, and Frequency Control

system of the chicken embryo via a chorioallantoic membrane vein using a glass capillary needle [43]. The chicken embryo and the chorioallantoic membrane, still attached to the yolk, was submerged inside a beaker of 37°C PBS solution (Fig. 2 c). The sparse spiral array was placed on top of the embryo with a standoff distance of 3 cm, and coupled to the embryo and the chorioallantoic membrane via the PBS. The viability of the embryo was monitored by visual inspection of the heartbeat through the ultrasound images during the experiment. Data acquisition and post-processing parameters can be found in Table I.

III. Results

A. Transmit field simulations

Fig. 3 summarizes the results of transmit field simulations. When transmitting an un-steered 30° divergent wave using all elements, the field was non-uniform in space and contained multiple unwanted tails behind the main wave front (Fig. 3 a). When 5 steered diverging waves (±5° in azimuth and elevation directions) were simulated and synthetically compounded, the wavefront was more uniform across the field of view (Fig. 3 b). By limiting the number of transmitting elements to 120, the uniformity of the field in lateral and axial directions improved either when transmitting a single wave (Fig. 3 c), and after angular compounding of 5 diverging waves (Fig. 3 d). For the latter case, in particular, the secondary lobes behind the main wave front were further reduced compared to all previously discussed cases. This transmission sequence was able to maintain the field homogeneity (standard deviation of the field of view at 3 cm and 20° opening angle: ±0.6 dB) while covering a large field of view, where the overlapping sector for the 5 steered transmits was 20°, and the largest sector covered by any beam was up to 40°. When transmitting with 120 elements, the maximum pressure in the compounded pressure field was 5.3 dB lower than when transmitting with 256 elements in this simulation. The 2-D pressure field at 3 cm depth was also measured using the hydrophone. The maximum MI and peak-to-peak pressure were 0.05 and 115 kPa respectively. The low pressures were to avoid bubble destruction. All the results have been obtained using this sequence.

B. Straight vessel phantom experimental results

Fig. 4 shows the volumetric rendering of microbubbles inside the 1 mm diameter vessel beamformed using both DAS and SC methods. Qualitatively the volumetric rendering of the DAS beamformed volume contained higher levels of clutter than the SC beamformed volume; as introduced in Section I, this clutter is originating from the *microbubble* scatter and is a direct result of the sparsity of the elements in the probe. Hence, this clutter can neither be avoided by tissue clutter suppression techniques, nor by microbubble-specific pulsing sequences like amplitude modulation or pulse inversion. On the other hand, the SC beamforming suppresses this clutter as the clutter signal has lower spatial coherence than the primary echoes from the

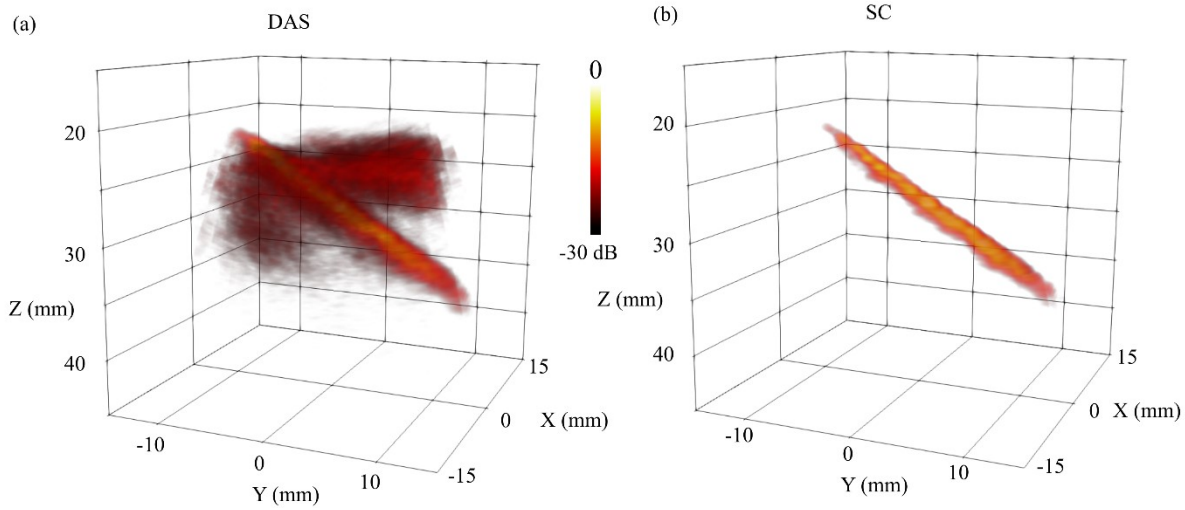

Fig. 4. Renders of 5 angles compounded, 50-frames averaged volumes of microbubbles in the straight vessel phantom. RF data was filtered to attenuate the PVA signal, then (a) delay-and-sum (DAS) and (b) spatial coherence (SC) beamforming were performed on the same dataset, shown to their maximum intensities and 30 dB dynamic range.

This article has been accepted for publication in a future issue of this journal, but has not been fully edited. Content may change prior to final publication. Citation information: DOI 10.1109/TUFFC.2021.3086597, IEEE Transactions on Ultrasonics, Ferroelectrics, and Frequency Control

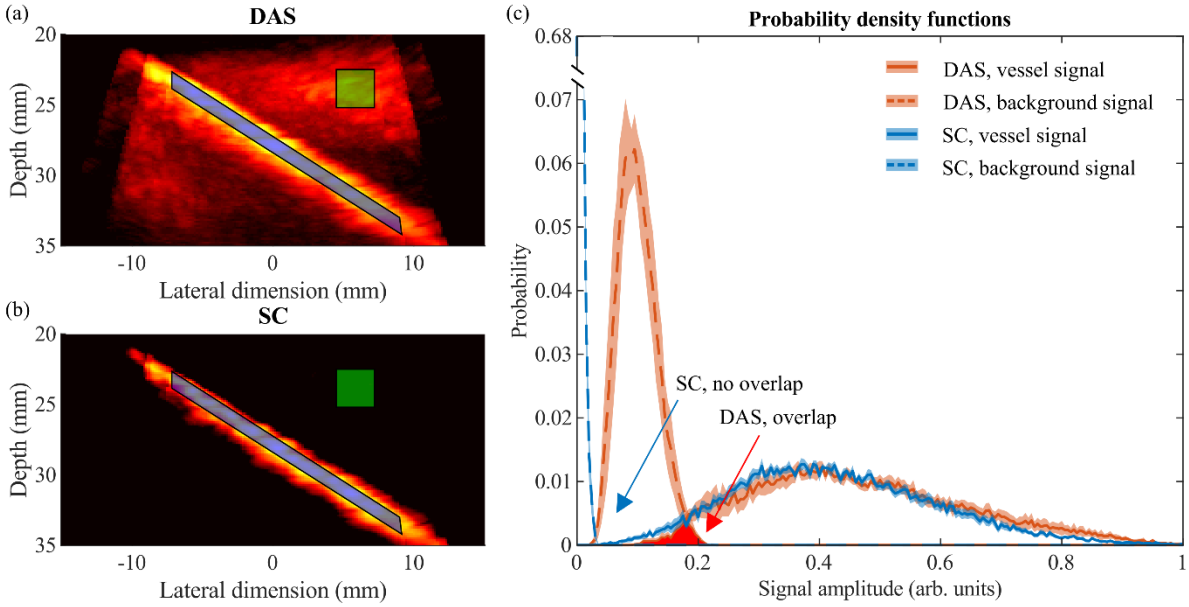

Fig. 5. Assessment of the generalized contrast to background ratio (GCBR) for a compounded volume. Cross-sections of the cylindrical vessel mask and the cubical background mask displayed on top of maximum intensity projections of 50-frames averaged, 5-angle compounded volumes beamformed using the (a) delay-and-sum (DAS) and (b) spatial coherence (SC) method. (c) normalized histograms of the signal within these two regions for both methods. There is an overlap between vessel and background histograms for the DAS beamformed volume but not for the SC beamformed volume. Shaded areas are standard error of 7 measurements.

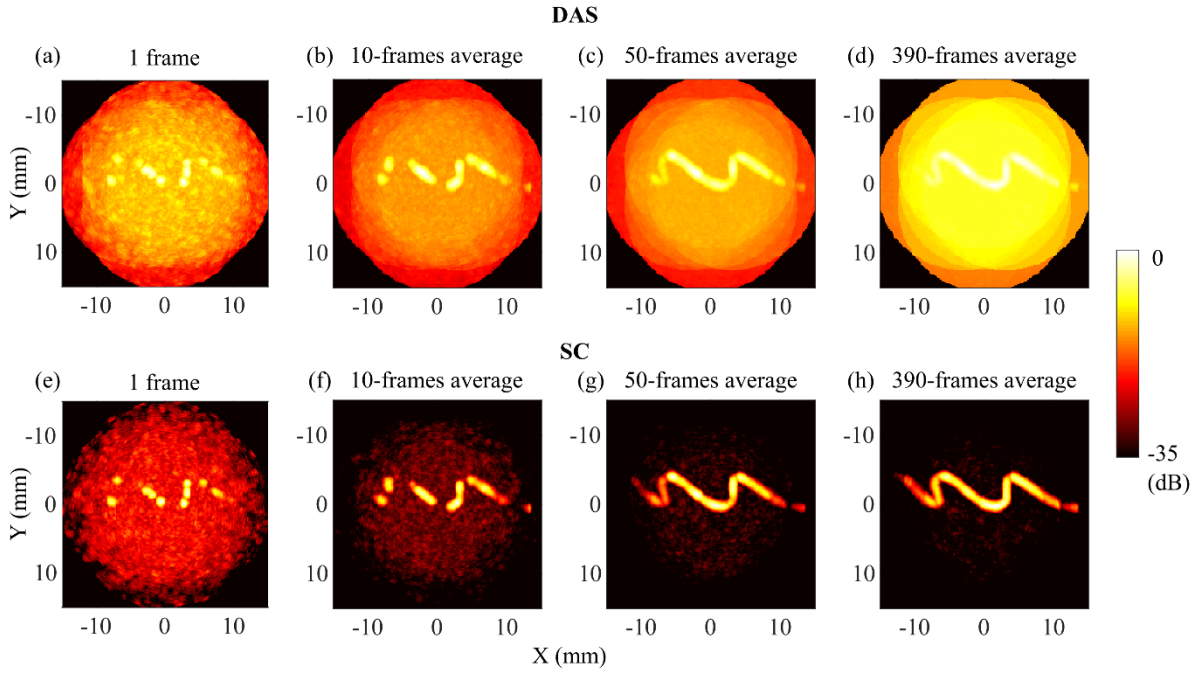

Fig. 6. Maximum intensity projection onto the XY-plane beamformed using (a-d) delay-and-sum (DAS) and (e-h) spatial coherence (SC). PVA signal was attenuated prior to beamforming. Averaging an increasing number of volumetric frames from 0 to 3.9 seconds (1 to 390-frames average at 100 Hz rate) reveals the helical shape as microbubbles flow through the vessel. All images are normalized to their maximum intensity.

microbubbles.

Quantitative evaluations of the image quality for both beamforming methods using the masked regions are shown in Fig. 5 a and b. The mean and standard error of the traditional contrast to background ratios of the SC and DAS beamformed volumes were

This article has been accepted for publication in a future issue of this journal, but has not been fully edited. Content may change prior to final publication. Citation information: DOI 10.1109/TUFFC.2021.3086597, IEEE Transactions on Ultrasonics, Ferroelectrics, and Frequency Control

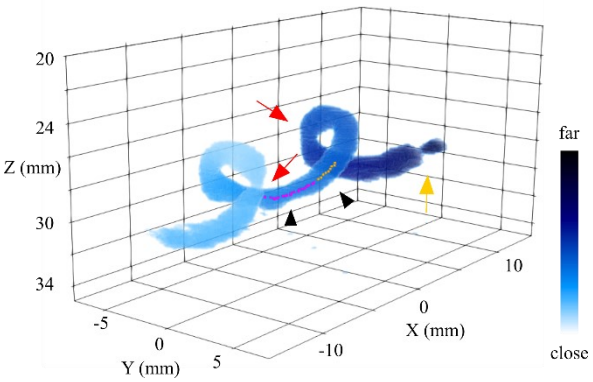

Fig. 7. volume render of a 390-frame averaged spatial coherence volume for 3.9 seconds duration. Two sample tracks of super-localized microbubble positions are overlayed on top of the time-averaged volume (black arrowheads point to the purple and yellow bubble location dots). The 3-D helical shape of the vessel is clearly visible. To enhance visualization, this render shows only signal above -30 dB. The color map corresponds to distance to the spatial location (x = -15, y = 0, z = 20 mm). Non-overlapping regions of the transmit beams are not cropped out in this render. The yellow arrow indicates an artefact caused by non-overlapping transmit beams. Red arrows indicate two locations where the vessel diameter appears slightly underestimated.

38.5 ± 0.5 dB and 13.6 ± 0.2 dB, respectively. As shown in Fig. 5 c, for the SC beamformed volume, there was no overlap between the vessel and background probability density functions (GCBR = 1), whereas for the DAS beamformed volumes, there was some overlap between signal from the two regions (GCBR = 0.98).

C. Helical micro-vessel experimental results

Fig. 6 shows the results from the helical vessel experiment. Single microbubbles could be seen moving through the micro-vessel in both the SC and DAS beamformed volumes, albeit with much higher contrast in the SC volumes. By averaging an increasing number of DAS (incoherently) and SC frames in time, the trajectory of the microbubbles within the vessel could be shown. The helical shape of the vessel became apparent as the positions of moving microbubbles were accumulated (Fig. 6 d, h). The background level in SC decreases as more frames were averaged, whereas the background level of DAS increased. Since the background distribution after the coherence calculation was centered around zero, the spread of this distribution decreased as more frames were averaged, leading to a decrease in the mean of its envelope-detected intensity distribution. Stanziola *et al.* have observed a similar increase in signal to background level for the coherence images [27]. On the other hand, the background level of the DAS volumes appeared to increase. This is because fewer bubbles were present in the vessel towards the end of the recording. Combined with the low number of bubbles, the DAS averaged bubble signal decreased while the background level stayed constant, leading to the background level increase after normalization.

Fig. 7 shows a rendering of the average volume after 3.9 seconds accumulation. The final volume was mostly uniform in diameter except for two locations (Fig. 7 red arrows). Single microbubbles could be tracked between frames to calculate microbubble velocity. Fig. 7 shows two examples of such tracks (black arrowheads). The flow speed estimated from tracking 24 microbubbles in the SC beamformed volume was 20.9 ± 7.6 mm/s, which agreed with the true velocity, expected to be between 16.5 and 23.6 mm/s.

D. Chicken embryo vascular imaging results

Fig. 8 shows the results of the *in vivo* chicken embryo experiment. Inside the PBS solution, the yolk

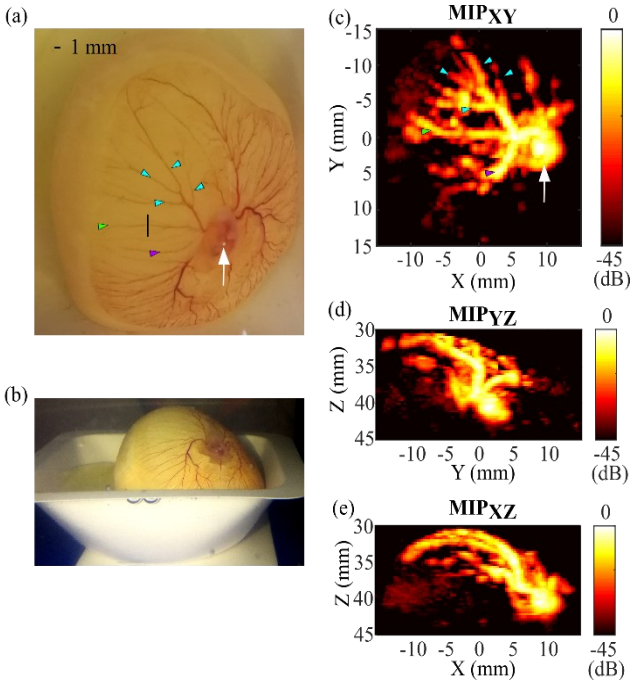

Fig. 8. (a-b) Photographs of the chicken embryo with the yolk submerged in a PBS solution as seen from the (a) the top and (b) the side. (a) Chorioallantoic membrane vessel diameter was estimated to be 0.35 mm at one location (black line) using the full width half maximum of the photograph's intensity. (b) The yolk assumes its ovoid shape when submerged, which can be seen when looking from the side. (c-d) Maximum intensity projections of the ultrasound volumetric render, beamformed using the SC beamformer. All tissue signal was removed prior to beamforming by using an SVD filter. By comparing (a) the top view of the photograph and (c) the maximum intensity projection of the ultrasound image in depth, the heart (white arrow) and some branches of the chorioallantoic membrane vessels can be identified and matched (blue, green, and purple triangular arrowheads). Air bubbles in the PBS solution above the yolk were cropped out manually in (c-e).

assumed its natural ovoid shape, which can be seen when looking at the two photographs taken from the top and side (Fig. 8 a, b). The chicken embryo and its chorioallantoic membrane blood vessels are distributed on the surface of the yolk, creating a dome-like shape. After averaging all SC beamformed frames, the shape of the blood vessels can be seen from the maximum intensity projections of the ultrasound volumetric image (Fig. 8 c-e). By comparing the photograph (Fig. 8 a) and the maximum intensity projection from the top (Fig. 8 c), the heart and the chorioallantoic blood vessels patterns could be identified and matched. A landmark in the ultrasound image is also identified on the photograph (Fig. 8 a black line). By looking at the gray scale intensity across the length of the labeled black line on the photograph, we have estimated the diameter of the blood vessel at this location to be 350 µm. This figure shows that the imaging scheme can detect blood vessels at this size *in vivo*.

IV. Discussion

In this paper, we propose to use a sparse spiral array combined with spatial coherence beamforming to reach a uniform transmit field, sufficient SNR, and low clutter levels to achieve microbubble high frame rate volumetric imaging. The low SNR caused by low transmitted field pressure due to the few number of elements is compatible with high frame rate microbubble imaging, where mid-range pressure intensities (at what is normally used for line-by-line imaging) can lead to bubble destruction. To improve the transmitted field non-uniformity, the central, more densely populated elements were used. Combined with angular compounding, a uniform transmitted field, in space and time, was obtained (Fig. 3). The SC beamformer further separates microbubble clutter from microbubble signal by exploiting the coherence of signals. We included all lags in the coherence to better differentiate between microbubble signal (high spatial coherence) and microbubble clutter and noise (low spatial coherence) after the removal of 'tissue' signal. A more detailed analysis of the spatial coherence is in the Appendix.

With the spiral array-specific transmission strategy combined with the SC beamforming method, we have achieved high quality volumetric contrast images at two microbubble concentrations *in vitro*. Fig. 4 and 5 compare the beamforming methods for the 1 mm vessel at high microbubble concentrations. The improvement in image quality can be visualized in Fig. 4, where the background clutter signal is significantly reduced for the SC beamformed volume. There is also no overlap between vessel and background signal distributions for the SC volume as opposed to the DAS volume, cf. Fig. 5, and quantified by a GCBR of 1, and 0.98, respectively. This indicates that the tissue clutter is suppressed for the SC beamformed volumes, and the improvement in image quality is not only due to alterations in dynamic range. For applications where it is important to distinguish microbubble signal and background signal (for example in perfusion detection) the improvements in image quality offered by the SC beamformer can be beneficial.

At low microbubble concentrations, individual microbubbles could be tracked in time (Fig. 7). Because of the good separation of background and microbubble signal distributions, automatic bubble detection is easier using the SC beamformed volume. Similar processing methods can be applied to enable super-resolution and volume flow rate measurements.

The SC beamformed volumes also have the advantage that they can be directly averaged through time (Fig. 6). Since SC beamformed images do not contain phase information, frames with microbubble displacement do not interfere when averaged. The noise distribution of the coherence calculation is centered around 0, thus the background intensity level (post tissue signal removal) tends to 0 when more frames are averaged [27]. This enables vascular mapping in low signal to noise ratio scenarios and is especially suited with the sparse array. The background level in the DAS beamformed volumes instead increased, due to fewer microbubbles being visible towards the end of the acquisition (perhaps due to microbubble destruction), while the subsequent normalization increased the background level. Moreover, averaging in DAS needed to be applied in the envelope domain in order to not reduce microbubble signal by coherent, destructive summation. This however also means that the background levels will never reduce [27].

In the final averaged SC volume, the helical vessel diameter appears uniform in the entire field of view except for at two locations (Fig. 7 red arrows). This is probably because the transmit field at those locations was still not perfectly uniform, despite the results found in simulation. The discrepancy between simulation and experiment is likely due to the transducer element variations in production. The uniformity of the transmit field due to transducer element variations can be improved by increasing the number of compounded angles (at the cost of frame rate) or improving the elements' consistency through the manufacturing process.

This article has been accepted for publication in a future issue of this journal, but has not been fully edited. Content may change prior to final publication. Citation information: DOI 10.1109/TUFFC.2021.3086597, IEEE Transactions on Ultrasonics, Ferroelectrics, and Frequency Control

Fig. 8 illustrates vasculature imaging of the chicken embryo and its chorioallantoic membrane. The heart as well as larger vessels stemming from the heart are clearly visible. Some of the smaller branches of the chorioallantoic membrane vessels can also be identified and matched to the photograph. In the top view maximum intensity projection, vessels can be seen extending across the entire field of view (Fig. 8 a, c, green and blue arrows). However other smaller branches are incomplete or missing (< 350 µm). A possible reason may be that the slow microbubble flow in these vessels were removed by the SVD filter. The wide range of blood flow velocity (1 µm/s to 1 mm/s [44]) within these vessels leads to difficulty in preserving all flow velocities.

One of the common reservations to the use of advanced beamformers is computation time. SC beamforming adds one additional step (correlation calculation) on top of the conventional DAS beamforming algorithm. When tested on a computer with 512 GB RAM 24 Cores CPU running at 10% load, the correlation calculation step adds approximately 1.3 s, i.e., +50%, to the beamforming algorithm for a 3 × 3 × 1.5 cm volume of 520251 voxels in total (same dimension as the chicken embryo acquired volume). This additional computation time may also be reduced by parallel computing or Graphical Processing Units (GPU) implementations. Divergent transmit wave imaging using the spiral array allows volumetric imaging of large field of views at high frame rates. A final frame rate of 1 kHz was used in this study, which could be increased to the depth-limited pulse repetition frequency by combining the compounding angles in a sliding fashion. High frame rate imaging not only offers higher temporal resolution, but also the flexibility in performing advanced post-processing techniques. They become particularly important in *in vivo* scenarios where tissue motion is significant.

Another possibility for tissue suppression is the use of microbubble-specific pulsing schemes. The bandwidth of our prototype probe is 40%, which is not wide enough to sense the higher harmonics. However, non-linear fundamental pulsing schemes should be investigated [45]. Exploiting the non-linear behavior of microbubbles for tissue suppression can simplify both the post-processing and the threshold selection for the advanced beamformers [46]. The high frame rate that can be reached with the sparse spiral array can reduce motion-related artefacts to reach better cancelation of various pulses.

Since the sparse array elements have one-to-one connections to the ultrasound machine, it can be used for more complex pulse sequence designs. For example, high resolution focused-beam volumetric images can be acquired prior to or post high frame rate acquisitions to provide more structural information. High resolution 2-D images can be acquired and displayed in real time by transmitting focused-beams onto 2-D planes, providing anatomical information to clinicians to better position their probe and reduce drift. The ability to steer in 3-D space could also be exploited for blood flow assessment by spectral Doppler measurement at specific locations [47]. The adaptability of the sparse spiral array makes it a potentially powerful tool for clinical applications and a promising solution for relatively cheap 3-D systems for the experimental test of new methods.

V. Conclusion

In this paper, we have presented the results of high frame rate volumetric imaging of microbubbles in *in vitro* experiments and *in vivo*. We have shown that using a spiral array-specific transmission scheme (the center 120 elements were used to generate divergent waves with 30° opening angle at 0° and 5° steering angles) combined with the spatial coherence beamformer yielded high quality volumetric contrast images and the ability to visualize single microbubbles.

Appendix

The spatial correlation of each receive channel pair was calculated for both high and low microbubble concentration *in vitro* experiments. Fig. A1 displays the results. One frame of each datasets was used to select one voxel with microbubble and one voxel from the background region. The locations of these voxels are marked on the maximum intensity projections (Fig. A1 (a, b)). For each voxel, the 256 channels give a total of 32639 channel pairs, and the non-normalized correlation of each pair of elements ($sc_{voxel}(i,j)$) was calculated according to Eq. A1, which is equivalent to Eq. 1 without the summations and normalization:

$$sc_{voxel}(i,j) = s(i)s^*(j), \quad i,j \in [1,256], i \neq j \tag{A1}$$

where $s(i)$ is the signal received by channel/element i, i and j are non-repeating element indexes. A zoomed-in version of all correlations is displayed relative to their element-to-element distances (Fig. A1 (c,d)). Since the pair-wise correlation values are noisy, the data was binned into 17 bins, each containing 2000 values, and the means are displayed (Fig. A1 (c,d)

This article has been accepted for publication in a future issue of this journal, but has not been fully edited. Content may change prior to final publication. Citation information: DOI 10.1109/TUFFC.2021.3086597, IEEE Transactions on Ultrasonics, Ferroelectrics, and Frequency Control

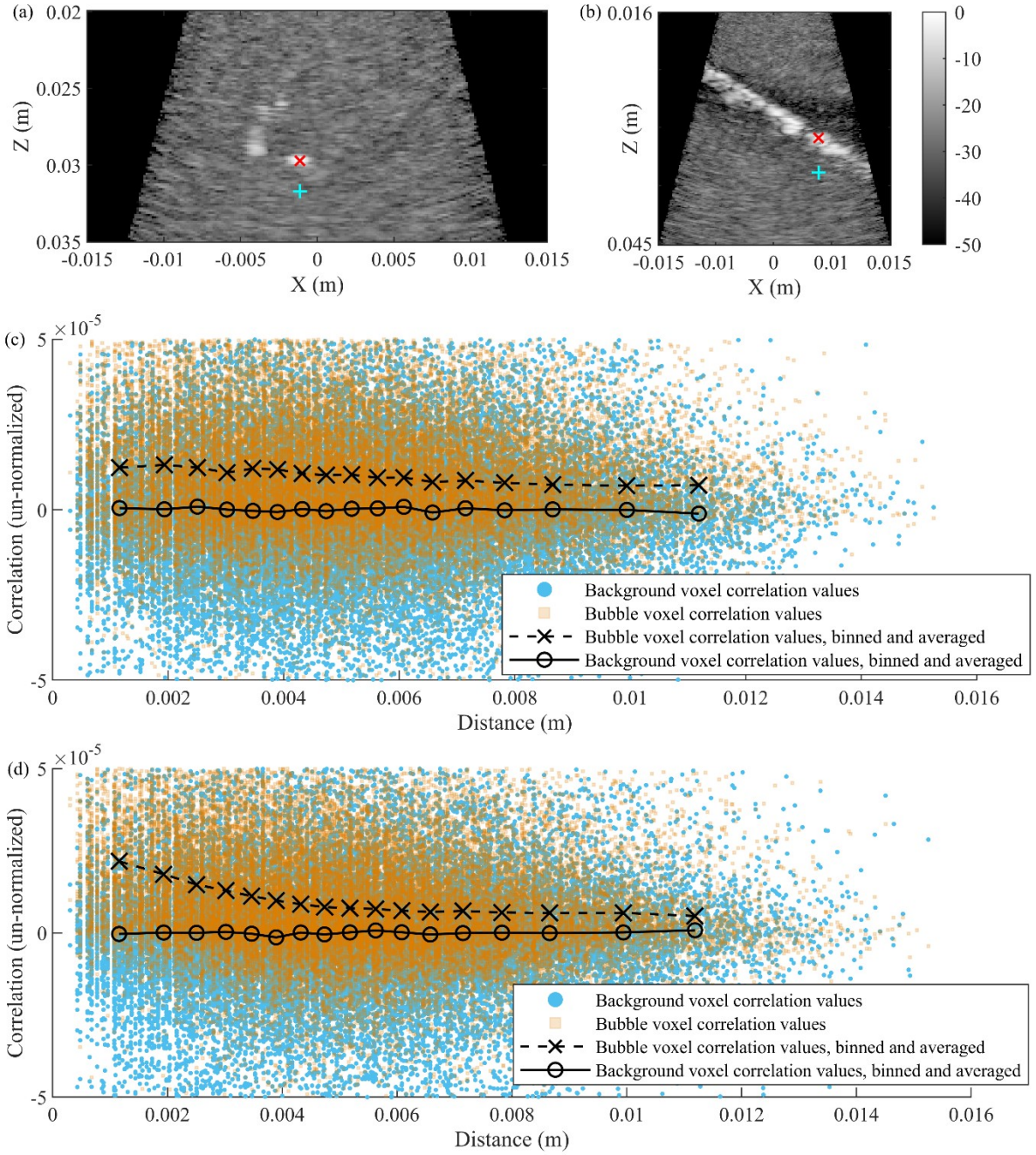

Figure A1: (a-b) Maximum intensity projections onto the X-Z plane (from one frame) for the previously described low concentration helical vessel experiment (a) and the high concentration vessel experiment (b). One voxel containing microbubble signal (red × sign) and one voxel containing background signal (turquoise + sign) were selected for the calculation of element-to-element correlation values (c-d). Channel pair-wise correlation values for the low (c) and high (d) concentration experiments are plotted (orange and turquoise datapoints) against the element-to-element distances. Every 2000 datapoints were binned and averaged (black lines). The y-axes are set to a limited range for better visualization.

black lines). For all element distances, the binned and averaged background voxel correlation values were around 0. This result is to be expected because the 'tissue' signal was attenuated using the SVD filter, therefore the background region contained mainly uncorrelated noise. At both microbubble concentrations, the binned correlations values were positive for the bubble-containing voxels and decreased as the element-to-element distance increases. The single microbubble acts as a coherent

scatterer, and the decrease in correlation is expected to be influenced by noise. At high concentrations, the correlation decrease can be due to both noise and interference of adjacent microbubbles. These trends are consistent as previously described in [28]. Since microbubble voxel correlations was higher than the background voxel correlations for all element-to-element distances, all distances were used in the spatial coherence calculations.

ACKNOWLEDGEMENTS

The authors would like to thank Robert Beurskens and Dr. Jasper Schoormans (both Erasmus MC) for the discussions and support. We also acknowledge Andrea Traversi and Filippo Piccardi (University of Florence, Italy and Delft University of Technology, the Netherlands) for their contributions to the probe development and setup. This work is part of the research programme "Vernieuwingsimpuls – Vidi 2017" with project number QUANTO-16572, which is (partly) financed by the Dutch Research Council (NWO). All animal experiments were conducted in accordance with the Netherlands Experiments on Animals Act and in accordance with the European Council (2010/63/EU) on the protection of animal use for scientific purposes.

REFERENCES

[1] M. Claudon *et al.*, "Guidelines and good clinical practice recommendations for contrast enhanced ultrasound (CEUS) in the liver – update 2012," *Ultrasound Med. Biol.*, vol. 39, no. 2, pp. 187–210, Feb. 2013.

[2] R. Senior *et al.*, "Contrast echocardiography: evidence-based recommendations by European Association of Echocardiography," *Eur. J. Echocardiogr.*, vol. 10, no. 2, pp. 194–212, Aug. 2008.

[3] P. Frinking, T. Segers, Y. Luan, and F. Tranquart, "Three decades of ultrasound contrast agents: a review of the past, present and future improvements," *Ultrasound Med. Biol.*, vol. 46, no. 4, pp. 892–908, Apr. 2020.

[4] I. G. Newsome and P. A. Dayton, "Visualization of microvascular angiogenesis using dual-frequency contrast-enhanced acoustic angiography: a review," *Ultrasound Med. Biol.*, vol. 46, no. 10, pp. 2625–2635, Oct. 2020.

[5] K. Christensen-Jeffries *et al.*, "Super-resolution ultrasound imaging," *Ultrasound Med. Biol.*, vol. 46, no. 4, pp. 865–891, Apr. 2020.

[6] H. J. Vos *et al.*, "Contrast-enhanced high-frame-rate ultrasound imaging of flow patterns in cardiac chambers and deep vessels," *Ultrasound Med. Biol.*, vol. 46, no. 11, pp. 2875–2890, Nov. 2020.

[7] C. Rabut *et al.*, "4D functional ultrasound imaging of whole-brain activity in rodents," *Nat. Methods*, vol. 16, no. 10, pp. 994–997, Oct. 2019.

[8] J. Zhu *et al.*, "3D super-resolution US imaging of rabbit lymph node vasculature in vivo by using microbubbles," *Radiology*, vol. 291, no. 3, pp. 642–650, Jun. 2019.

[9] B. Heiles *et al.*, "Ultrafast 3D ultrasound localization microscopy using a 32 x 32 matrix array," *IEEE Trans. Med. Imaging*, vol. 38, no. 9, pp. 2005–2015, Sep. 2019.

[10] L. Petrusca *et al.*, "A new high channels density ultrasound platform for advanced 4D cardiac imaging," in *Proc. IEEE Ultrason. Symp.*, 2017.

[11] J. Janjic *et al.*, "A 2-D ultrasound transducer with front-end ASIC and low cable count for 3-D forward-looking intravascular imaging: performance and characterization," *IEEE Trans. Ultrason. Ferroelectr. Freq. Control*, vol. 65, no. 10, pp. 1832–1844, Oct. 2018.

[12] P. Santos, G. U. Haugen, L. Lovstakken, E. Samset, and J. D'hooge, "Diverging wave volumetric imaging using subaperture beamforming," *IEEE Trans. Ultrason. Ferroelectr. Freq. Control*, vol. 63, no. 12, pp. 2114–2124, Dec. 2016.

[13] F. Fool *et al.*, "3D high frame rate flow measurement using a prototype matrix transducer for carotid imaging," *Proc. IEEE Ultrason. Symp.*, 2019.

[14] C. E. Morton and G. R. Lockwood, "Theoretical assessment of a crossed electrode 2-D array for 3-D imaging," in *Proc. IEEE Ultrason. Symp.*, 2003, vol. 1, pp. 968–971.

[15] S. Holbek, T. L. Christiansen, M. B. Stuart, C. Beers, E. V. Thomsen, and J. A. Jensen, "3-D vector flow estimation with row–column-addressed arrays," *IEEE Trans. Ultrason. Ferroelectr. Freq. Control*, vol. 63, no. 11, pp. 1799–1814, Nov. 2016.

[16] J. Yu, H. Yoon, Y. M. Khalifa, and S. Y. Emelianov, "Design of a volumetric imaging sequence using a Vantage-256 ultrasound research platform multiplexed with a 1024-element fully sampled matrix array," *IEEE Trans. Ultrason. Ferroelectr. Freq. Control*, vol. 67, no. 2, pp. 248–257, Feb. 2020.

[17] M. Bernal, B. Cunitz, D. Rohrbach, and R.

Daigle, "High-frame-rate volume imaging using sparse-random-aperture compounding," *Phys. Med. Biol.*, vol. 65, no. 17, p. 175002, Sep. 2020.

[18] A. Ramalli, E. Boni, A. S. Savoia, and P. Tortoli, "Density-tapered spiral arrays for ultrasound 3-D imaging," *IEEE Trans. Ultrason. Ferroelectr. Freq. Control*, vol. 62, no. 8, pp. 1580–1588, Aug. 2015.

[19] A. Ramalli *et al.*, "High-frame-rate tri-plane echocardiography with spiral arrays: From simulation to real-time implementation," *IEEE Trans. Ultrason. Ferroelectr. Freq. Control*, vol. 67, no. 1, pp. 57–69, Jan. 2020.

[20] S. Harput *et al.*, "3-D super-resolution ultrasound imaging with a 2-D sparse array.," *IEEE Trans. Ultrason. Ferroelectr. Freq. Control*, vol. 67, no. 2, pp. 269–277, Feb. 2020.

[21] S. Harput *et al.*, "Quantitative microvessel analysis with 3-D super-resolution ultrasound and velocity mapping," in *Proc. IEEE Ultrason. Symp.*, 2020.

[22] E. Roux, F. Varray, L. Petrusca, C. Cachard, P. Tortoli, and H. Liebgott, "Experimental 3-D ultrasound imaging with 2-D sparse arrays using focused and diverging waves," *Sci. Rep.*, vol. 8, no. 1, pp. 1–12, Dec. 2018.

[23] J. E. Chomas, P. Dayton, D. May, and K. Ferrara, "Threshold of fragmentation for ultrasonic contrast agents," *J. Biomed. Opt.*, vol. 6, no. 2, pp. 141–151, 2001.

[24] M. A. Averkiou, M. F. Bruce, J. E. Powers, P. S. Sheeran, and P. N. Burns, "Imaging methods for ultrasound contrast agents," *Ultrasound Med. Biol.*, vol. 46, no. 3, pp. 498–517, Mar. 2020.

[25] L. Nie, D. M. J. Cowell, T. M. Carpenter, J. R. McLaughlan, A. A. Cubukcu, and S. Freear, "Motion compensation for high-frame-rate contrast-enhanced echocardiography using diverging waves: image registration versus correlation-based method," in *Proc. IEEE Ultrason. Symp.*, 2019, vol. 2019-Oct., pp. 380–383.

[26] A. Stanziola *et al.*, "Motion artifacts and correction in multipulse high-frame rate contrast-enhanced ultrasound," *IEEE Trans. Ultrason. Ferroelectr. Freq. Control*, vol. 66, no. 2, pp. 417–420, Feb. 2019.

[27] A. Stanziola, C. H. Leow, E. Bazigou, P. D. Weinberg, and M.-X. Tang, "ASAP: super-contrast vasculature imaging using coherence analysis and high frame-rate contrast enhanced ultrasound," *IEEE Trans. Med. Imaging*, vol. 37, no. 8, pp. 1847–1856, Aug. 2018.

[28] M. A. Lediju, G. E. Trahey, B. C. Byram, and J. J. Dahl, "Short-lag spatial coherence of backscattered echoes: imaging characteristics," *IEEE Trans. Ultrason. Ferroelectr. Freq. Control*, vol. 58, no. 7, pp. 1377–1388, Jul. 2011.

[29] D. Hyun, L. Abou-Elkacem, V. A. Perez, S. M. Chowdhury, J. K. Willmann, and J. J. Dahl, "Improved sensitivity in ultrasound molecular imaging with coherence-based beamforming," *IEEE Trans. Med. Imaging*, vol. 37, no. 1, pp. 241–250, Jan. 2018.

[30] D. Hyun, G. E. Trahey, M. Jakovljevic, and J. J. Dahl, "Short-lag spatial coherence imaging on matrix arrays, part I: beamforming methods and simulation studies," *IEEE Trans. Ultrason. Ferroelectr. Freq. Control*, vol. 61, no. 7, pp. 1101–1112, Jul. 2014.

[31] M. Jakovljevic, B. C. Byram, D. Hyun, J. J. Dahl, and G. E. Trahey, "Short-lag spatial coherence imaging on matrix arrays, part II: phantom and in vivo experiments," *IEEE Trans. Ultrason. Ferroelectr. Freq. Control*, vol. 61, no. 7, pp. 1113–1122, Jul. 2014.

[32] H. J. Vos *et al.*, "Sparse volumetric PZT array with density tapering," in *Proc. IEEE Ultrason. Symp.*, 2018.

[33] E. Boni, A. C. H. Yu, S. Freear, J. A. Jensen, and P. Tortoli, "Ultrasound open platforms for next-generation imaging technique development," *IEEE Trans. Ultrason. Ferroelectr. Freq. Control*, vol. 65, no. 7, pp. 1078–1092, Jul. 2018.

[34] J. A. Jensen and N. B. Svendsen, "Calculation of pressure fields from arbitrarily shaped, apodized, and excited ultrasound transducers," *IEEE Trans. Ultrason. Ferroelectr. Freq. Control*, vol. 39, no. 2, pp. 262–267, Mar. 1992.

[35] J. A. Jensen, "Field: a program for simulating ultrasound systems," in *the 10th Nordicbaltic Conference on Biomedical Imaging*, 1996, vol. 34, no. 1, pp. 351–353.

[36] C. Demené *et al.*, "Spatiotemporal clutter filtering of ultrafast ultrasound data highly increases Doppler and fUltrasound sensitivity," *IEEE Trans. Med. Imaging*, vol. 34, no. 11, pp. 2271–2285, Nov. 2015.

[37] R. Mallart and M. Fink, "The van Cittert-Zernike theorem in pulse echo measurements," *Cit. J. Acoust. Soc. Am.*, vol. 90, p. 2718, 1991.

[38] A. Rodriguez-Molares *et al.*, "The ultrasound toolbox," in *Proc. IEEE Ultrason. Symp.*,

2017.

[39] M. van der Ven, J. J. Luime, L. L. van der Velden, J. G. Bosch, J. M. W. Hazes, and H. J. Vos, "High-frame-rate power Doppler ultrasound is more sensitive than conventional power Doppler in detecting rheumatic vascularisation," *Ultrasound Med. Biol.*, vol. 43, no. 9, pp. 1868–1879, Sep. 2017.

[40] A. Rodriguez-Molares *et al.*, "The generalized contrast-to-noise ratio: a formal definition for lesion detectability," *IEEE Trans. Ultrason. Ferroelectr. Freq. Control*, vol. 67, no. 4, pp. 745–759, Apr. 2020.

[41] V. Daeichin *et al.*, "Microbubble composition and preparation for high-frequency contrast-enhanced ultrasound imaging: in vitro and in vivo evaluation," *IEEE Trans. Ultrason. Ferroelectr. Freq. Control*, vol. 64, no. 3, pp. 555–567, Mar. 2017.

[42] O. Couture and V. Hingot, "Short course: super-resolution ultrasound," *IEEE Ultrason. Symp*, 2020.

[43] B. Meijlink, I. Skachkov, A. F. W. van der Steen, N. de Jong, and K. Kooiman, "The preparation of chicken ex ovo embryos and chorioallantoic membrane vessels as in vivo model for contrast-enhanced ultrasound imaging and microbubble-mediated drug delivery studies.," *J. Vis. Exp.*, vol. 1, no. 168, p. 27, 2021.

[44] A. Kloosterman, B. Hierck, J. Westerweel, and C. Poelma, "Quantification of blood flow and topology in developing vascular networks," *PLoS One*, vol. 9, no. 5, p. e96856, May 2014.

[45] P. J. Phillips, "Contrast pulse sequences (CPS): imaging nonlinear microbubbles," *Proc. IEEE Ultrason. Symp.*, vol. 2, pp. 1739–1745, 2001.

[46] J. Baranger, B. Arnal, F. Perren, O. Baud, M. Tanter, and C. Demene, "Adaptive spatiotemporal SVD clutter filtering for ultrafast Doppler imaging using similarity of spatial singular vectors," *IEEE Trans. Med. Imaging*, vol. 37, no. 7, pp. 1574–1586, Jul. 2018.

[47] A. Ramalli *et al.*, "Real-time system for 3D Doppler spectral analysis with sparse arrays," *presented at the IEEE Ultrason. Symp.* 2020.

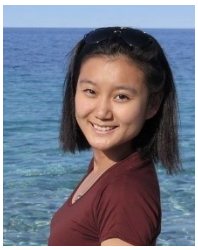

Luxi Wei (M'19) received her B.Sc. degree in honours biophysics from the University of British Columbia, Canada, in 2016 and her M.Sc. degree in medical biophysics from the Univiersity of Toronto, Canada, in 2019. She is currently pursuing a Ph.D. degree at the Department of Biomedical Engineering, Erasmus Medical Center, The Netherlands. Her research includes high frame rate ultrasound, contrast agent imaging, volumetric beamforming techiniques, and transducer development.

Geraldi Wahyulaksana was born in Jakarta, Indonesia in 1992. He got the M.S. degree in electrical engineering from Eindhoven University of Technology, in 2017 after working on contrast agent modelling for MRI. From 2017 to 2019 he worked as a software designer in Son and developed an object detection system for a wireless power transfer system with air-coupled ultrasound. Since 2019 he is currently a Ph.D. student at the Department of Biomedical Engineering, Erasmus Medical Center, Rotterdam, The Netherlands. His current research interest is methods to detect microbubbles with high framerate ultrasound imaging.

Bram Meijlink received his B.Sc. and M.Sc. degrees in Biomedical Sciences with a specialization in Regenerative Medicine and Technology from Utrecht University, Utrecht, The Netherlands in cooperation with Eindhoven Technical University, Eindhoven, The Netherlands, in 2016 and 2019 respectively. He is currently pursuing a Ph.D. degree with the Department of Biomedical Engineering, Erasmus Medical Center, Rotterdam, The Netherlands. His thesis focuses on obtaining more insight into the interaction between vibrating microbubbles, the vessel wall, and drugs in 3D *in vitro* and *in vivo* models in order to improve microbubble-mediated drug delivery for cardiovascular diseases and cancer.

Alessandro Ramalli (S'10–M'12–SM'19) was born in Prato, Italy, in 1983. He received the master's degree in electronics engineering from the University of Florence, Florence, Italy, in 2008; the joint Ph.D. degree in electronics system engineering and in automation, systems and images from the University of Florence and the University of Lyon, Lyon, France, respectively, in 2012. From 2012 to 2017, he was involved in the development of the imaging section of a programmable open ultrasound system by the University of Florence. From 2017 to 2019, he worked as a Post-Doctoral Researcher with the Laboratory of Cardiovascular Imaging and Dynamics, KU Leuven, Leuven, Belgium, granted by the European Commission through a "Marie Skłodowska-Curie Individual Fellowships". Here, he developed high frame rate imaging techniques for echocardiography. Currently he is a research fellow at the University of Florence and his research interests include medical imaging, echocardiography, beamforming methods, ultrasound simulation, arrays and systems design.

Emile Noothout completed his education at the Intermediate Technical School for Mechanics, Dordrecht, The Netherlands, in 2004. From 2004 to 2006, he was with Leidse Instrumentmaker School, Leiden, The Netherlands, where he studied for Research Instrument Maker. From 2007 to 2013, he was a Research Instrument Maker with TNO, Delft, The Netherlands, where he developed hardware for space and lithography. Since 2008, he has been involved in developing and building ultrasound transducers for the petrochemical industries. Since 2013, he has been with the Delft University of Technology, Delft, where he is involved in the development of medical ultrasound transducers and research assistance.

Martin D. Verweij (M'10) received the M.Sc. (cum laude) and Ph.D. degrees in electrical engineering from Delft University of Technology, Delft, The Netherlands, in 1988 and 1992, respectively. From 1993 to 1997, he was a Research Fellow with the prestigious Royal Netherlands Academy of Arts and Sciences, Amsterdam, The Netherlands. In 1995 and 1997 he was a Visiting Scientist at Schlumberger Cambridge Research, Cambridge, England. In 1998 he became an Assistant Professor, and later that year an Associate Professor, with the Laboratory of Electromagnetic Research, Delft University of Technology. In 2011 he switched to the Laboratory of Medical Imaging at the same university, where he became Head Ultrasound Research in 2021. Since 2015 he also has a part-time position at the Biomedical Engineering group, Erasmus Medical Centre, Rotterdam.

His research interests include dedicated transducer design, beamforming algorithms, the mathematical modeling and numerical simulation of ultrasound, and the physics of ultrasound. He is the originator of the Iterative Nonlinear Contrast Source (INCS) method for the computation of nonlinear ultrasound fields. Dr. Verweij is a research leader of the Dutch Technology Foundation (TTW-NWO) on projects involving transducer design, beamforming and imaging. He is a Fellow of the Acoustical Society of America, Associate Editor of the Journal of the Acoustical Society of America, and treasurer of the Dutch Society for Medical Ultrasound.

Enrico Boni (M'12) was born in 1977 in Florence, Italy. He graduated in electronic engineering on 2001 at the University of Florence, Italy and received the PhD degree in Electronic System Engineering on 2005 from the University of Florence, Italy. He currently holds a Research position at the Microelectronic System Design Laboratory, Department of Information Engineering, University of Florence, Italy. His research interests include analog and digital systems design, digital signal processing algorithms, digital control systems, Doppler ultrasound signal processing, microemboli detection and classification.

Klazina Kooiman (SM'18) received the M.Sc. degree (cum laude) in biopharmaceutical sciences specializing in pharmaceutical technology from Leiden University, Leiden, The Netherlands, and the Ph.D. degree in ultrasound contrast agents for therapy from the Department of Biomedical Engineering, Thoraxcenter, Erasmus MC University Medical Center Rotterdam, the Netherlands, in 2011. In 2018, she acquired the prestigious ERC starting grant from the European Research Council, and in 2019 the prestigious Vidi Grant from the Netherlands Organization for Scientific Research, domain Applied and Engineering Sciences. She is currently an

Associate Professor and the Head of the Therapeutic Ultrasound Contrast Agent Group, Department of Biomedical Engineering, Thoraxcenter, Erasmus MC University Medical Center, focusing on using ultrasound contrast agents for drug delivery and molecular imaging. Dr. Kooiman was a recipient of the EFUSMB 2011 Young Investigator Award, Vienna, Austria. She is the co-director of the Annual European Symposium on Ultrasound Contrast Imaging, Rotterdam, which is attended by approximately 180 scientists from universities and industries all over the world.

Antonius F. W. van der Steen (Fellow, IEEE) received the master's degree in applied physics and the Ph.D. degree in medical sciences. He is currently the Head of Biomedical Engineering at the Thorax Centre, Erasmus MC. He is an expert in ultrasound, cardiovascular imaging, and cardiovascular biomechanics. He has a career at the crossroads of Engineering, Health Care, and Industry. He has experience in running large consortia as the Co-Founder and former Chairman of the Medical Delta, which comprises of over 280 scientists working on technical solutions for sustainable health. He was also the Co-PI of ParisK, one of the large CTMM projects (16 MEuro). His international profile is high, with more than 200 invited lectures all over the world, and Guest Professorship/Guest Researcher in Canada, Japan, and China. Dr. van der Steen is a fellow of the European Society of Cardiology. He is a member of the Netherlands Academy of Technology (AcTI) and a board member of the Royal Netherlands Academy of Sciences (KNAW). He is a recipient of the Simon Stevin Master Award, and the NWO PIONIER Award in Technical Sciences.

Piero Tortoli (M'91-SM'96-F'19) received the Laurea degree in electronics engineering from the University of Florence, Italy, in 1978. Since then, he has been on the faculty of the Information Engineering Department at the same university, where he is currently full Professor of Electronics and was elected member of the Academic Senate. He is leading the Microelectronics Systems Design Laboratory. His research interests include the development of open ultrasound research systems and novel imaging/Doppler methods. On these topics, he has authored more than 300 papers.

Professor Tortoli is a Fellow of IEEE and AIMBE, "Docteur Honoris causa" of the University Claude Bernard Lyon 1, and an Honorary Member of the Polish Academy of Sciences. He has served on the IEEE International Ultrasonics Symposium Technical Program Committee since 1999 and is currently Associate Editor of the IEEE Transactions on Ultrasonics, Ferroelectrics, and Frequency Control. He chaired the 22nd International Symposium on Acoustical Imaging (1995), the 12th New England Doppler Conference (2003), established the Artimino Conference on Medical Ultrasound Technology in 2011 and organized it again in 2017.

Nico de Jong graduated from the Delft University of Technology, The Netherlands, in 1978. He received the M.Sc. degree in applied physics in the field of pattern recognition, and the Ph.D. degree in acoustic properties of ultrasound contrast agents, in 1993. From 2003 to 2011, he was a part-time Professor with the University of Twente in the group Physics of Fluids headed by Prof. Detlef Lohse. He is currently the Vice Head of Biomedical Engineering with the Thoraxcenter, Erasmus University Medical Center, Rotterdam, headed by Prof. Ton van der Steen. He is the Head of the Medical Imaging Group, Technical University, Delft. He is the Founder and an Organizer of the Annual European Symposium (this year for the 25th time, see http://www.echocontrast.nl) on ultrasound contrast imaging, held in Rotterdam and attended by approximately 175 scientists from universities and industries all over the world. He is on the safety committee of the World Federation of Ultrasound in Medicine and Biology (WFUMB). He is an Associate Editor of Ultrasound in Medicine and Biology and the IEEE Transactions on Ultrasonics, Ferroelectrics, and Frequency Control. He has been a guest editor for special issues of several journals. He teaches on Technical Universities and the Erasmus MC. He has graduated 38 Ph.D. students and is currently supervising more than 12 Ph.D. students.

Hendrik J. Vos (M '14) received the M.Sc. degree in Applied Physics from Delft University of Technology, Delft, The Netherlands in 2004, and his Ph.D. degree with the Department of Biomedical Engineering at Erasmus MC, Rotterdam, The Netherlands, in 2010. He worked as a Postmaster Researcher with the University of Florence, Italy, and as a contract researcher for the petrochemical industry on cutting-edge ultrasonic solutions. He currently is associate professor with Erasmus MC and Delft University of Technology, and received a Dutch NWO-TTW-VIDI personal grant in 2018. His research interests include acoustical array technology for biomedical imaging in all its aspects: transducers, 2-D and 3-D beamforming, cardiac shear waves, ultrafast Doppler, contrast imaging, and related subclinical and clinical studies.